Supplementary Information for

Brain-wide interactions during hippocampal sharp wave ripples

Noam Nitzan[1], Rachel Swanson[1] Dietmar Schmitz[2] and György Buzsáki[1,3,*]

[1]Neuroscience Institute, Langone Medical Center, New York University, New York, NY 10016; [2]Charité-Universitätsmedizin Berlin, Corporate member of Freie Universität Berlin, Humboldt-Universität zu Berlin, and Berlin Institute of Health, Neuroscience Research Center, Berlin, Germany. [3]Department of Neurology, Langone Medical Center, New York University, New York, NY 10016

Corresponding author: György Buzsáki
Email: gyorgy.buzsaki@nyumc.org

This PDF file includes:
Methods
Supplemental Figures 1-8
Supplemental Movie
References for SI reference citations

SI Materials and Methods

Neuropixels data

For all analyses presented in the paper, we use data from the Allen Brain Institute Visual Coding dataset publicly available at https://allensdk.readthedocs.io/en/latest/visual_coding_neuropixels.html, which we refer to throughout the paper as AI dataset. Data included both male and female mice of the following genotypes: 26 WT mice, 6 Pvalb-IRES-Cre/wt;Ai32(RCL-ChR2(H134R)_EYFP)/wt mice, 10 Sst-IRES-Cre/wt;Ai32(RCL-ChR2(H134R)_EYFP)/wt and 8 Vip-IRES-Cre/wt;Ai32(RCL-ChR2(H134R)-_EYFP)/wt mice. We modified the original probe labels provided by the Visual Coding dataset for 2 probed as follows probes: probe F -> probe C, probe C -> probe S. For Figure 3, we additionally used data from Steinmetz et al., (1), publicly available at https://figshare.com/articles/dataset/Eightprobe_Neuropixels_recordings_during_spontaneos_behaviors/7739750 which we refer to as UCL dataset. Data were downloaded as NWB files and converted to MATLAB format (Table S1).

Event detection

Ripples were detected by filtering (110-200) the raw LFP (sampled at 1250 Hz) using a 3rd order Butterworth filter. The signal was rectified and normalized to yield a ripple power time series. Ripple detection was restricted to epochs were the speed of the animal was below 2 cm/s for at least 2 seconds. Putative ripple events were defined as those were the beginning/end cutoffs exceeded 2 SDs and the peak power 3 SDs. We further included duration criteria of 15-250 ms. An additional 'noise' signal from a channel outside of the hippocampus was provided to exclude simultaneously occurring high frequency events. Ripple duration was calculated as the difference between stop and start times. The instantaneous ripple frequency was calculated by computing the analytical signal of the ripple-band filtered LFP using the Hilbert transform, unwarping the phase angles, applying median filtering and taking the difference between samples nearest the peak power bin of the ripple and dividing by 2 π. Ripples were visualized using spectrograms constructed using a complex Morlet wavelet transform with 4-12 logarithmically spaced cycles.
3-5 Hz cortical activity bouts were detected from the filtered (3-5 Hz) summed cortical MUA. Event peaks were identified similarly to ripples, without imposing a speed threshold.

Event triggered histograms

Ripple triggered peri-event time histograms (PETHs) were computed by counting spiking activity around peak ripple time into 1 ms (Fig. 3) or 10 ms bins (Fig. 5-6). The mean firing rate was then calculated by dividing by the bin size and number of ripples. PETHs were smoothed using a 10 ms Gaussian kernel. Units were deemed significantly SPW-R modulated using the same procedure described by Sosa et al. (2). In short, SPW-R times were jittered in a ± 1 s window to generate 1000 surrogate PETHs for each unit. We then calculated the sum of squared differences between the actual PETH and the mean of surrogate PETHs, and compared it to the sum of squared differences of each surrogate PETH with the mean of surrogate PETHs. Units were deemed

significantly modulated if this difference exceeded the 97.5 percentile, corresponding to p<0.05. The modulation sign (i.e., up or down-modulation) was computed by calculating the percent of firing rate change in a –50 ms to 200 ms window around SPW-R peak compared to a –1000 ms to –300 ms baseline window. This procedure was separately repeated for SPW-Rs detected on each probe. To better estimated the short time scale SPW-R effects (Figs. 5-6), PETHs were high-passed filtered at 0.5 Hz. We used principal component analysis (PCA), implemented using singular value decomposition, to extract the dominant neuronal response profiles that accounted for most of the variance in the PETHs. PCA was performed on the smoothed, z-scored PETHs and the coefficients were projected onto the data to obtain the low dimensional representations.

CSD analysis

For each probe in each session, we calculated the SPW-R triggered CSD in order to estimate the sharp wave amplitude. We used the inverse CSD method which is based on the inversion of the electrostatic forward solution (3).

Phase analysis

Phase was extracted using the filter-Hilbert method after filtering the raw LFP signals at either ripple (110-200 Hz) or theta (6-10 HZ) bands. Phase locking value was computed as $|n^{-1} \sum_{r=1}^{n} e^{ik_r}|$, where n is the total number of ripples and k is the phase angle at ripple r. Units were considered significantly phase modulated if their phase locking value was above 0.1, and their p-value on Rayleigh's test for circular non-uniformity was below 0.01.

Estimation of brain-state measures

Pupil data: Eye tracking data was acquired at 30 Hz and pre-processed by Siegle et al. (4). The pupil diameter, defined as the mean of the pupil height and width was normalized by the median of each session.

Power spectrum slope (PSS): We used the power spectrum slope as an estimate for brain state and cortical E/I balance (5). For each session, we selected an infragranular cortical channel and extracted the slope of the power spectrum between 4-100 Hz in a 2 seconds interval and a 50 ms sliding window.

State-index: The state-index (SI) was computed by shifting a moving window (0.5 s) along the binned (1 ms) and smoothed (30 ms Gaussian kernel SD) cortical MUA spikes and counting the proportion of nonzero bins (6, 7).

Mutual information estimation

Mutual information (MI) was estimated using the Neuroscience Information Theory Toolbox (https://github.com/nmtimme/Neuroscience-Information-Theory-Toolbox). In short, spiking data (from every two brain regions or single units) from ± 500 ms epochs around SPW-R peaks were counted into 10 ms bins and discretized into states using 4 (regions) or 2 (single units) uniform count bins. The MI, given by $\sum_{x\in X, y\in Y} p(x,y) log_2(\frac{(p(x,y))}{p(x)p(y)})$, was then computed for each time bin. We defined ΔMI as the average change in MI ± 50 ms around ripple peak or 0-300 ms post stimulus compared to baseline. The significance of MI estimation was tested by Monte Carlo

statistics using 5000 samples. Graphs were constructed from adjacency matrices binarized at a threshold of 1 SD. For brain region interactions (Fig. 4 A-B), we considered only significant MI values.

Hippocampal fiber projection analysis

To estimate the magnitude of hippocampal output to the various brain regions sampled in the datasets, we used imaging data from the Allen Mouse Brain Connectivity Atlas (http://connectivity.brain-map.org/). Our query for injections in hippocampal output structures (CA3/CA1/SUB) in wild-type animals, yielded 19 experiments (Exp. IDs: 116900714; 100147861; 120436274; 122641784; 120494729; 100148443; 113935285; 114429338; 127649005; 112308468; 112745073; 113166056; 272404772; 180523704; 127795906; 127222723; 152994878; 126523791; 640285199). We estimated the projection density by dividing the sum of detected pixels by the sum of all pixels in a given brain structure.

Classification of SPW-R location

We used a linear SVM trained using 10-fold cross validation to predict SPW-R location. Input features were normalized firing rate vectors from all units in a given session (excluding hippocampal units) surrounding SPW-Rs detected in dorsal CA1 (probes A-B) or posterior CA1 (probes D-E), but not both. Decoding accuracy is reported as the mean of the cross-validated accuracy. To obtain confidence intervals we randomly shuffled the data labels 1000 times.

Statistical analyses

Data were analyzed in Matlab (2021a). Throughout the paper, data are presented as mean ± s.e.m. or median ± median absolute deviance (MAD). Data are displayed as box plot representing median, lower and upper quartiles and whiskers representing most extreme data points. Statistical tests for multiple groups were performed either by effect size estimation computed using 5,000 bootstrapped resamples (Fig. 1B) according to the DABEST framework (8), or using Kruskal-Wallis test followed by Tukey-Kramer post hoc tests (Fig. 6C). For continuous measures (e.g., # of probes on which SPW-R was detected) we report the p-value from Pearson's correlation testing the null hypothesis of no correlation.

Code availability

The code used for this study was adapted from the buzcode repository (https://github.com/buzsakilab/buzcode) and the FMAT toolbox (http://fmatoolbox-.sourceforge.net/.)

Visualization

Brain images were generated using brainrenderer (9).

Data Availability

The AI data is available at https://allensdk.readthedocs.io/en/latest/visual_coding_neuropixels-.html.

The UCL data is available at https://figshare.com/articles/dataset/Dataset_from_Steinmetz_-et_al_-2019/9598406.

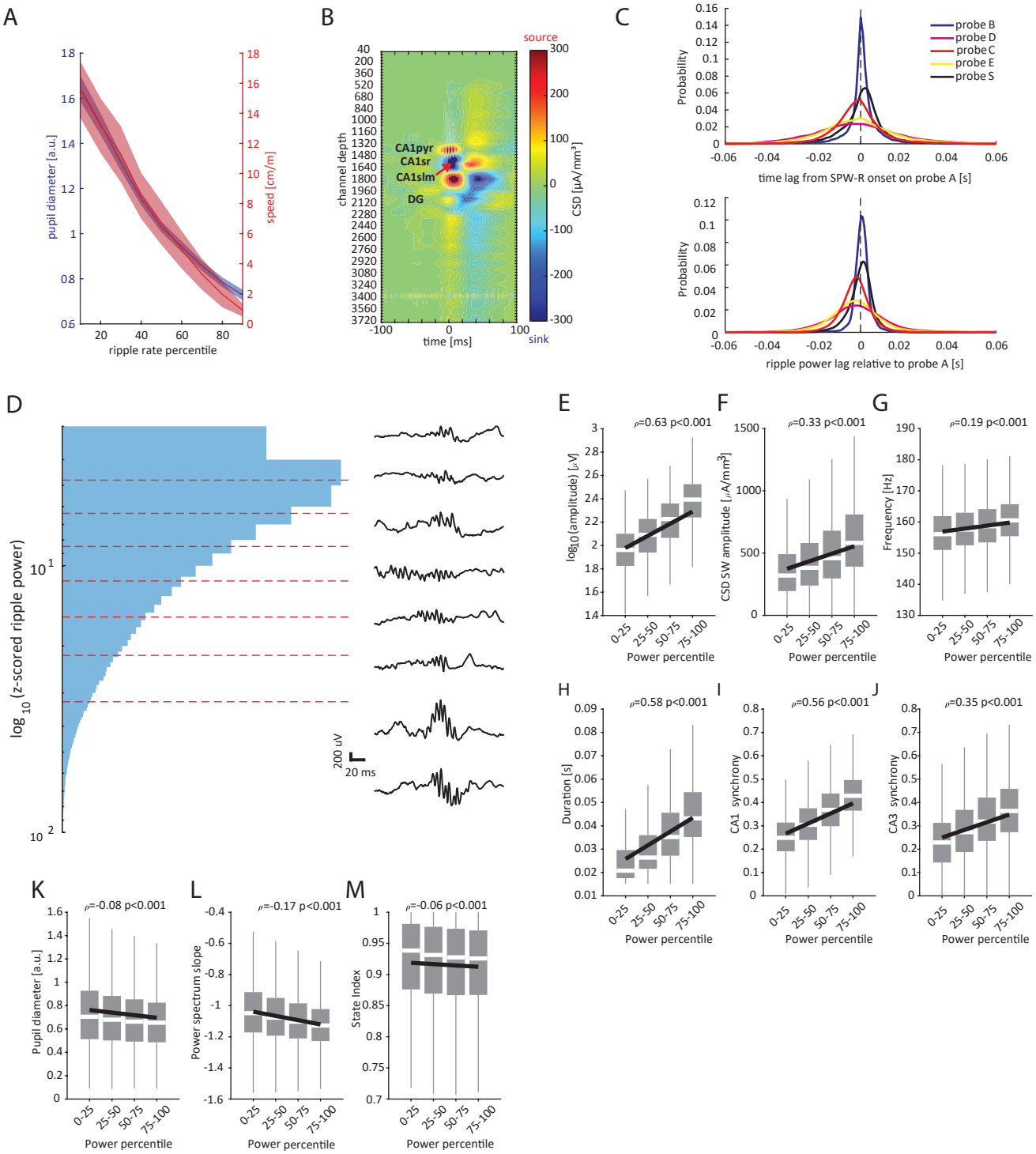
A
pupil diameter [a.u.]
speed [cm/m]
ripple rate percentile
B
source
sink
channel depth
CA1pyr
CA1sr
CA1slm
DG
time [ms]
CSD [μA/mm³]
C
probe B
probe D
probe C
probe E
probe S
Probability
time lag from SPW-R onset on probe A [s]
ripple power lag relative to probe A [s]
D
log 10 (z-scored ripple power)
200 uV
20 ms
E
ρ=0.63 p<0.001
log10(amplitude) [μV]
Power percentile
F
ρ=0.33 p<0.001
CSD SW amplitude [μA/mm²]
G
ρ=0.19 p<0.001
Frequency [Hz]
H
ρ=0.58 p<0.001
Duration [s]
I
ρ=0.56 p<0.001
CA1 synchrony
J
ρ=0.35 p<0.001
CA3 synchrony
K
ρ=-0.08 p<0.001
Pupil diameter [a.u.]
L
ρ=-0.17 p<0.001
Power spectrum slope
M
ρ=-0.06 p<0.001
State Index
0-25
25-50
50-75
75-100

Fig. S1. SPW-R features vary as a function of their amplitude. A) Pupil diameter (left y-axis, blue) and running speed (right y-axis, red), plotted as a function of SPW-R rate percentile (mean ± s.e.m; n = 45 and 50 sessions, respectively). B) SPW-R triggered CSD profile from one example session. Red arrow depicts maximal sharp wave amplitude in str. radiatum. C) Top: Distributions of time lags between SPW-R onset on probes B-E, S, and SPW-R onset on probe A (probe B: 0.8 ± 5.0 ms; probe C -1.6 ± 7.9 ms; probe D -2.4 ± 14.2 ms; probe E -1.6 ± 12.2 ms; probe S: 1.6± 7.5 ms; median ± MAD). Bottom: Distributions of event-wise ripple power time-series lags to maximal correlation, relative to probe A. Ripple power (110-220 Hz) was calculated for each SPW-R event on each probe in sessions where all 6 probes were used (probe B: 0.8 ± 2.0 ms; probe C -1.6 ± 4.6 ms; probe D 0 ± 9.1 ms; probe E -0.8 ± 7.7 ms; probe S: 0.8 ± 4.0 ms; median ± MAD; n = 95,338 events from 26 sessions). D) Ripples from all probes were classified based on their z-scored power octile (n = 347,525 events from 50 sessions). Left: histogram of ripple power from all sessions. Ripple power octiles are marked with red dashed lines. Right: example ripples from each octile. E-J) Distributions of ripple amplitude, sharp wave (SW) amplitude, ripple frequency, ripple duration and fractions of spiking CA1/ CA3 units for ripples of different quartiles. Pearson's correlation value and p-values are indicated in the top of each panel. K-M) Brain state measures including pupil diameter, power spectrum slope and state index for ripples of different quartiles.

Movie S1. Real time display of current flow (calculated using current source density analysis of the recorded voltages) surrounding SPW-R time, referenced to SPW-Rs detected in dorsal CA1. Red colors denote current sources; blue, current sinks. Note that ripple activity tends to begin at more posterior locations (right) and moves forward to septal direction (left) (n = 20148 recordings channels for which CCF coordinates were available; values shown are averaged across all SPW-Rs from the same session, n=50 sessions).

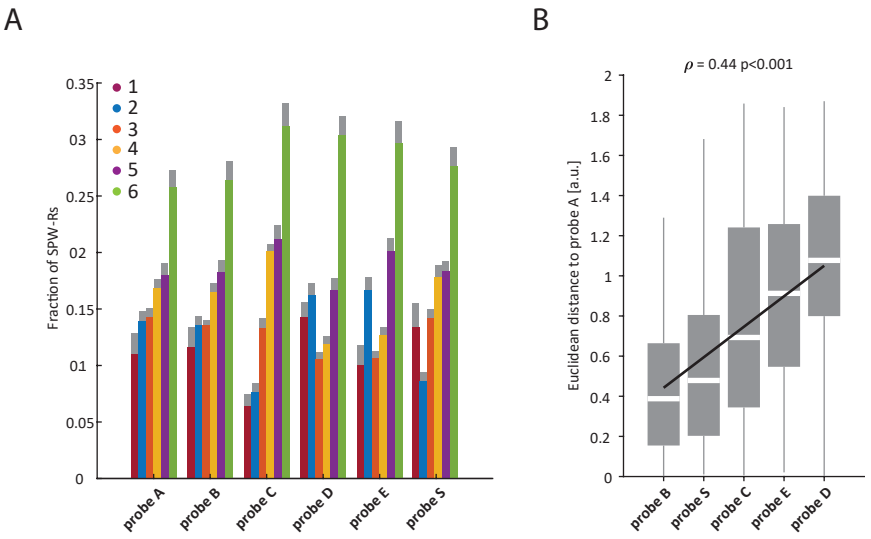

Fig. S2. Most SPW-Rs are synchronous in the recorded septal and posterior segments of the hippocampus. A) Average fractions of SPW-Rs detected on single to multiple probes (1 to 6), for SPW-Rs detected separately on each probe. Grey shaded area, s.e.m. Note that most SPW-Rs occurred simultaneously on all 6 probes. B) Box and whisker plots showing the distribution of Euclidean distances between the peak power principal components of all probes to probe A in all sessions, ordered according to physical distance from probe A. Rho and p-value are indicated on top (n = 224,083 events from 26 sessions where all probes were available).

Area name	# units	# sessions	Allen	UCL
Field CA1	6827	64	5840	987
Dentate gyrus	2334	62	1627	707
Subiculum	1441	33	849	592
Field CA3	1055	49	841	214
Prosubiculum	632	25	632	0
Field CA2	51	17	51	0
Postsubiculum	319	6	7	312
Infralimbic area	144	1	0	144
Taenia tecta	137	2	0	137
Retrosplenial area	267	3	0	267
Prelimbic area	582	7	0	582
Visual areas	19103	68	16283	2820
Anterior cingulate area	701	8	0	701
Secondary motor area	890	11	0	890
Orbital area	446	3	0	446
Olfactory areas	259	2	0	259
Posterior intralaminar thalamic nucleus	21	2	21	0
Central lateral nucleus of the thalamus	32	1	0	32
Intermediate geniculate nucleus	55	4	55	0
Mediodorsal nucleus of thalamus	397	3	0	397
Thalamus misc. nuclei	888	30	213	675
Subparafascicular nucleus	53	2	0	53
Posterior limiting nucleus of the thalamus	447	24	232	215
Lateral habenula	24	2	0	24
Medial geniculate complex	960	16	665	295
Intergeniculate leaflet of the lateral geniculate complex	53	5	53	0
Ethmoid nucleus of the thalamus	270	11	270	0
Lateral posterior nucleus of the thalamus	2977	48	2307	670
Suprageniculate nucleus	365	14	365	0
Posterior complex of the thalamus	960	13	313	647
Lateral dorsal nucleus of thalamus	185	5	41	144
Dorsal part of the lateral geniculate complex	1870	40	1414	456
Lateral septal nucleus	876	6	0	876
Nucleus accumbens	90	1	0	90
Medial septal nucleus	23	1	0	23
Olivary pretectal nucleus	27	4	27	0
Nucleus of the brachium of the inferior colliculus	43	1	0	43
Posterior pretectal nucleus	39	10	39	0
Anterior pretectal nucleus	1527	40	1280	247
Substantia nigra, reticular part	118	1	0	118
Midbrain misc. nuclei	531	27	193	338
Midbrain reticular nucleus	346	9	16	330

Table. S1. For each area included in the study, overall number of units, sessions and split into datasets

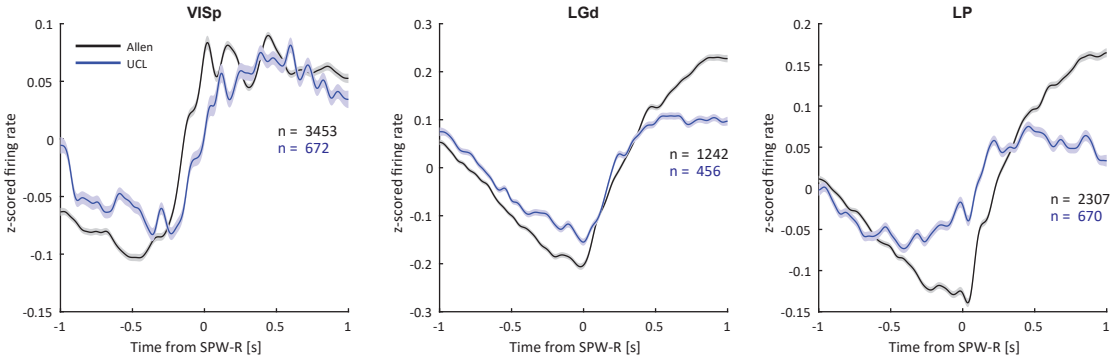

Fig. S3. Congruence between two data sets. SPW-R triggered PSTHs shown separately for the Allen (black) and UCL (blue) datasets for three example areas that were substantially sampled in both datasets. Note similar response profiles in the two datasets. Sample sizes indicated in each figure panel.

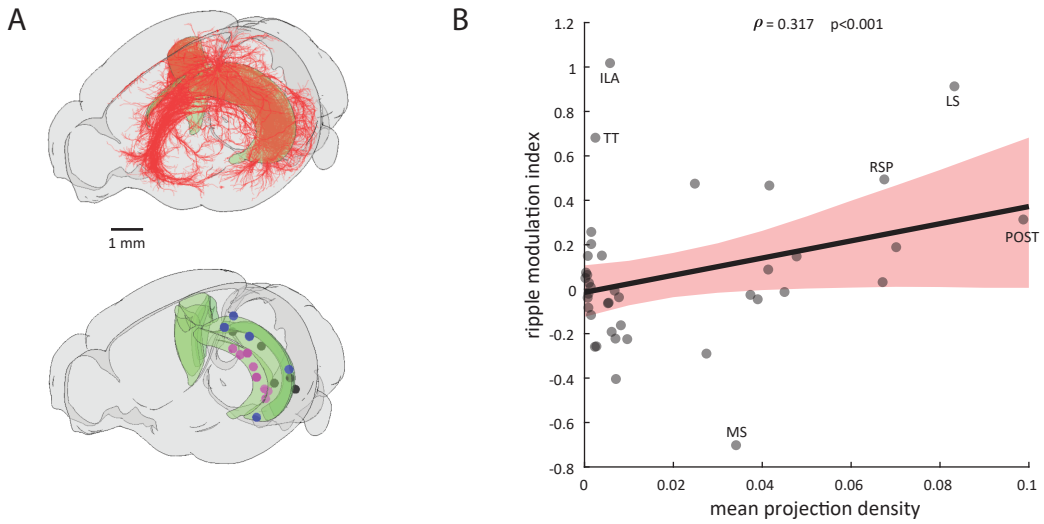

Fig. S4. Connectivity correlates with SPW-R response strength. A) Top: Cartoon showing the brain-wide distribution of hippocampal efferents (red) from areas CA3, CA1 and SUB. The hippocampus is shown in green. Bottom: visualization of dye injection coordinates. Blue, CA1 injections; Black, subicular injections; Magenta, CA3 injections (n=19). B) Ripple modulation (average response magnitude per area ± 30 ms around SPW-R peak) as a function of mean hippocampal projection density (averaged across 19 experiments in WT mice, Allen Institute mouse brain connectivity data). Least-squares fit line is depicted in black. Shaded area indicated 2.5% and 97.5% confidence bounds obtained from 5000 bootstraps. Pearson's rho and p-value are indicated on top.

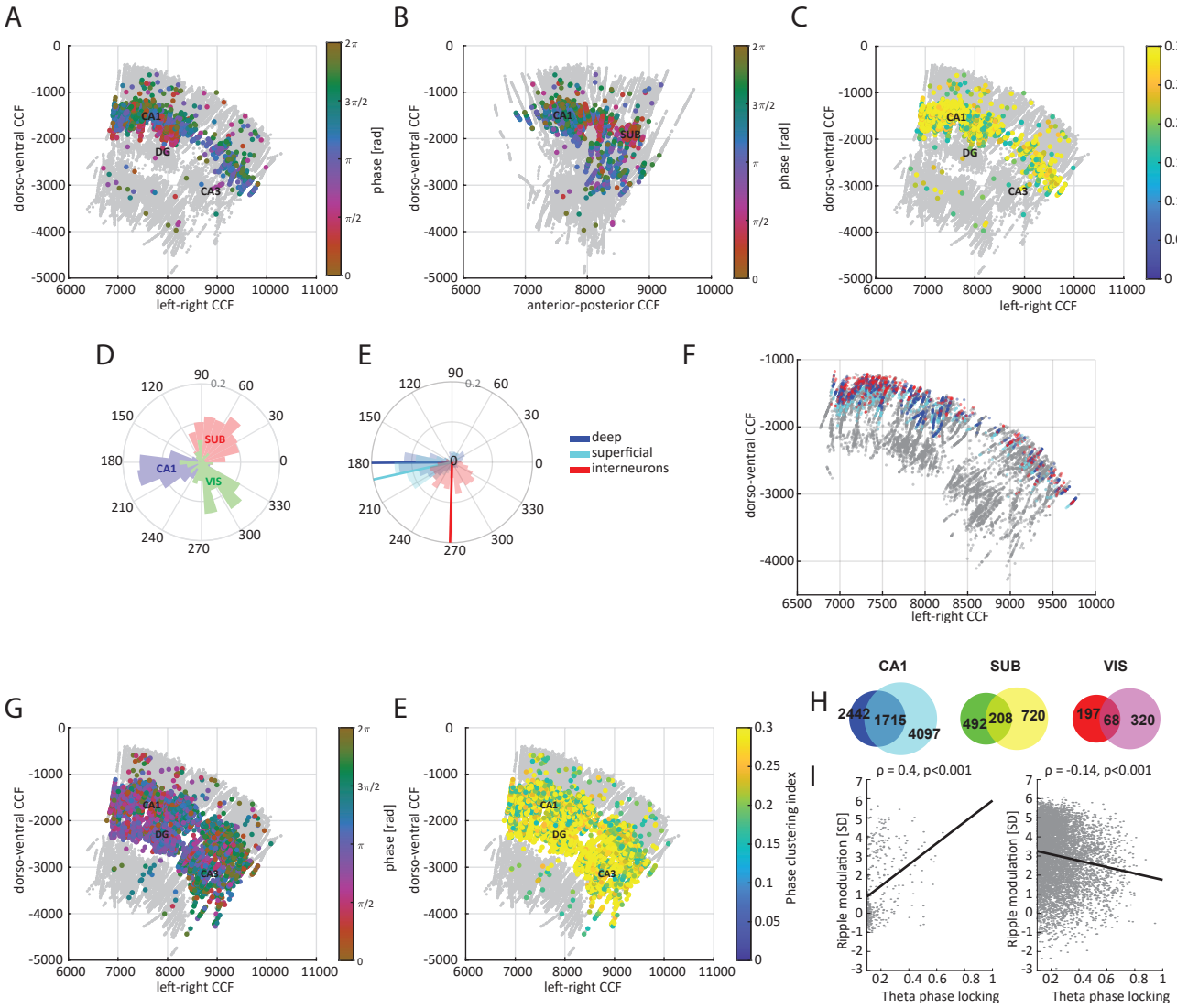

Fig. S5. Spatial variation of phase locking. A-B) Coronal (A) and sagittal (B) views of preferred ripple phase, calculated in reference to ripples recorded on probe A (dorsal CA1). Each dot represents one unit. Non-significantly modulated units are shown in grey (n = 3131/36156, Rayleigh test for circular non-uniformity). C) Coronal view of the resultant vector length. D) Phase distributions of preferred ripple phase for three major areas. Radial axis, probability. E) Ripple phase distributions of CA1 cells separated into deep and superficial pyramidal cells and interneurons. Bold lines point to the direction of mean vector for each population. Deep and superficial CA1 pyramidal cells are significantly different (p = 0.002; two-sample test for common median direction; n = 1278 deep and 970 superficial units). F) Locations of significantly modulated deep, superficial and interneurons in CCF coordinates. Same color coding as in (E). G) Same display as (A) but for theta oscillations. Analysis was restricted for periods where speed > 5 cm/s. E) Coronal view of resultant theta phase vector length. H) Venn diagrams showing the numbers of ripple (left) and theta (right) phase modulated units. I) Theta phase clustering index of significantly modulated cells, plotted against ripple modulation, for non-hippocampal (left) and hippocampal units (right). Black line: least-squares slope. Pearson's rho and p-values are indicated on the top of each panel.

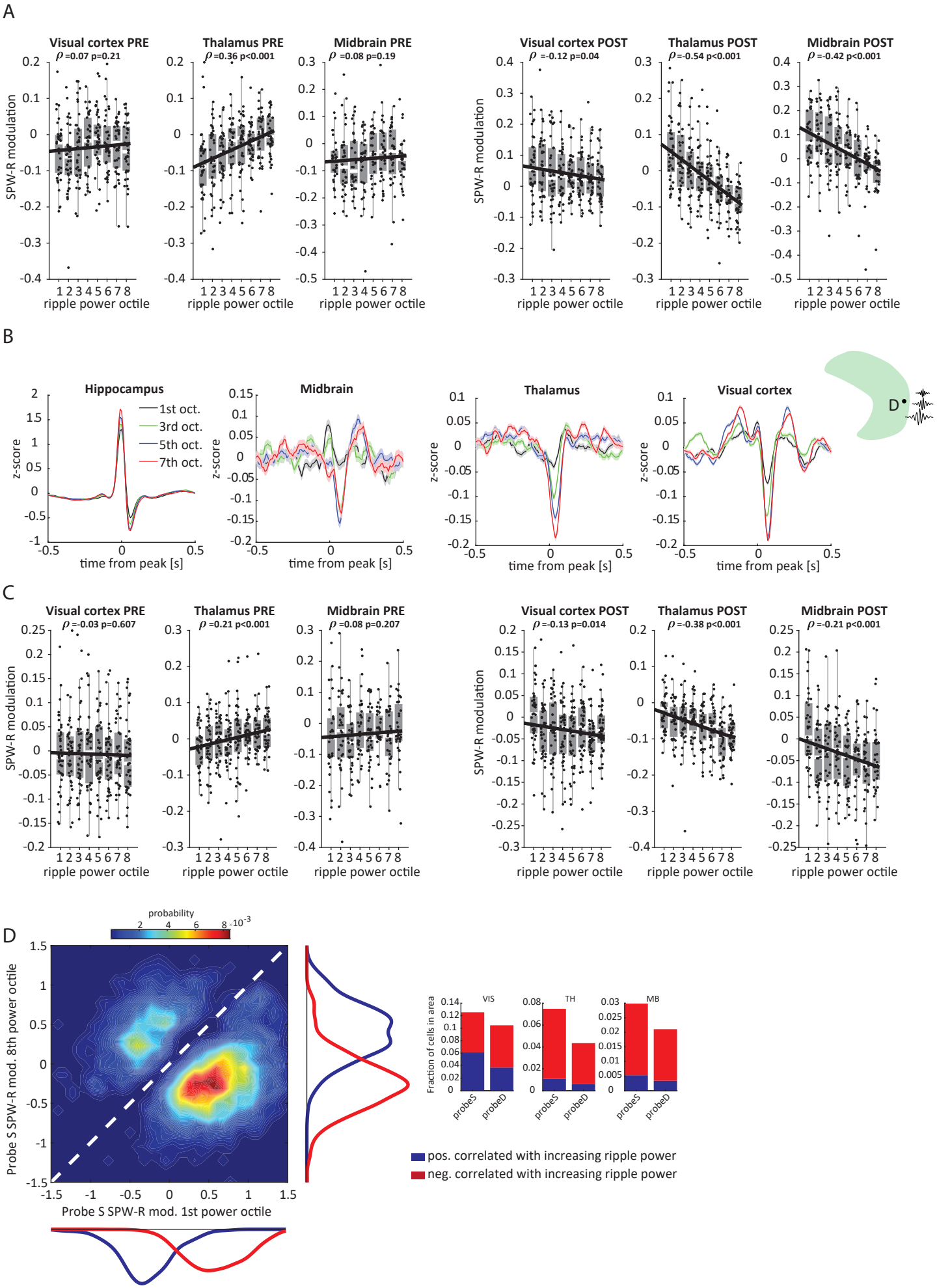
A
Visual cortex PRE
ρ =0.07 p=0.21
Thalamus PRE
ρ =0.36 p<0.001
Midbrain PRE
ρ =0.08 p=0.19
Visual cortex POST
ρ =-0.12 p=0.04
Thalamus POST
ρ =-0.54 p<0.001
Midbrain POST
ρ =-0.42 p<0.001
SPW-R modulation
ripple power octile
B
Hippocampus
1st oct.
3rd oct.
5th oct.
7th oct.
Midbrain
Thalamus
Visual cortex
z-score
time from peak [s]
D
C
Visual cortex PRE
ρ =-0.03 p=0.607
Thalamus PRE
ρ =0.21 p<0.001
Midbrain PRE
ρ =0.08 p=0.207
Visual cortex POST
ρ =-0.13 p=0.014
Thalamus POST
ρ =-0.38 p<0.001
Midbrain POST
ρ =-0.21 p<0.001
D
probability
Probe S SPW-R mod. 8th power octile
Probe S SPW-R mod. 1st power octile
Fraction of cells in area
VIS
TH
MB
probeS
probeD
pos. correlated with increasing ripple power
neg. correlated with increasing ripple power

Fig. S6. Magnitude of SPW-Rs affect target responses. A) Correlation between ripple power octile on probe S (shown in Fig. 5), averaged across all units from the same area and session, and pre- and post-SPW-R activity in partner regions (n = 38 sessions where probe S was available). B) SPW-R triggered PSTHs (mean ± s.e.m.), averaged across all neurons from the same brain region, triggered on SPW-Rs of increasing ripple power octile detected on probe D (posterior) (n = 31101 units from 42 sessions where probe D was available). C) Same as in A, for SPW-Rs on increasing ripple power octile on probe D. D) Left: density plot showing the joint distribution of extrahippocampal units whose SPW-R modulation significantly increased (data cloud above the diagonal) or decreased (data cloud below the diagonal) with increasing ripple power on probe S ($p<0.05$, two-tailed t-test against zero correlation). Marginal distributions are shown along the horizontal and vertical axes. Right: fractions of cells with significant positive or negative correlations from the target areas.

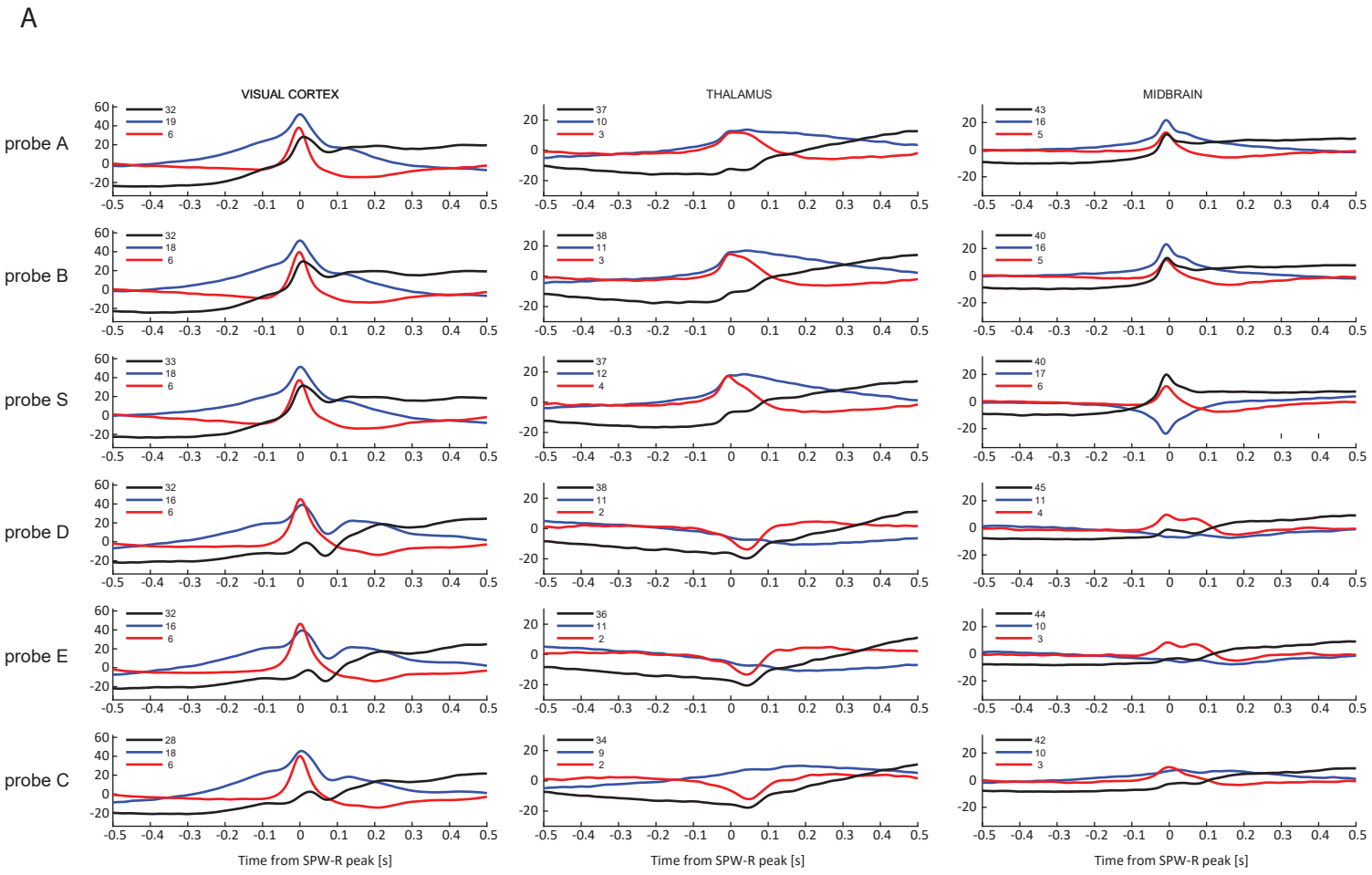
A
VISUAL CORTEX
THALAMUS
MIDBRAIN
probe A
probe B
probe S
probe D
probe E
probe C
Time from SPW-R peak [s]

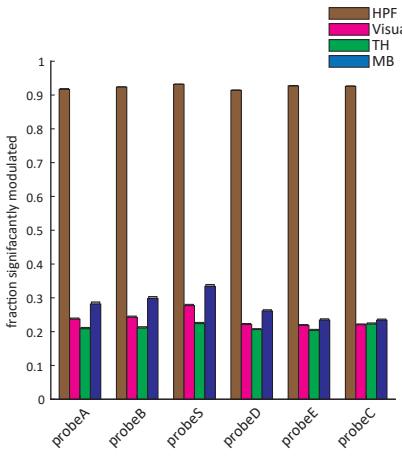
B
HPF
Visual cortex
TH
MB
fraction signifacantly modulated
probeA
probeB
probeS
probeD
probeE
probeC

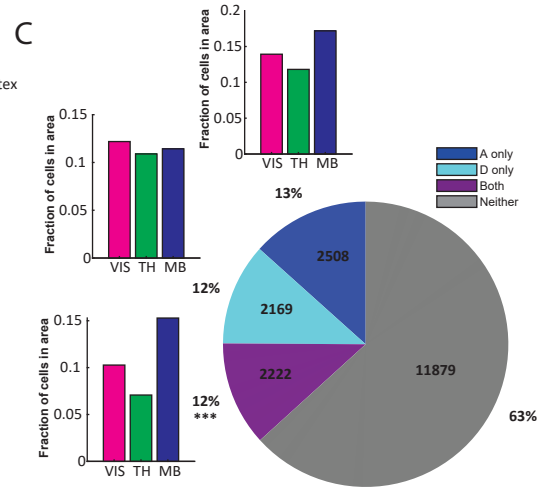
C
Fraction of cells in area
VIS TH MB
A only
D only
Both
Neither
13%
12%
12%
***
63%
2508
2169
2222
11879

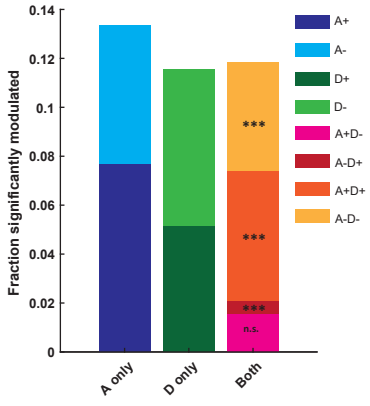
D
Fraction significantly modulated
A+
A-
D+
D-
A+D-
A-D+
A+D+
A-D-
***
n.s.
A only
D only
Both

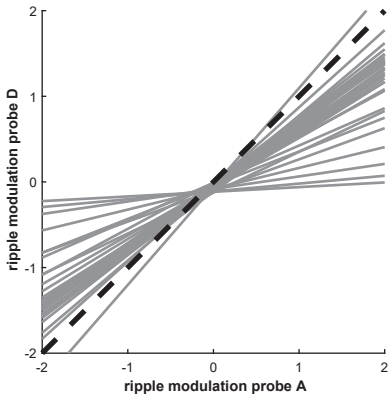
E
ripple modulation probe D
ripple modulation probe A

Fig. S7. **Spatial variation of SPW-R features by hippocampal segments**. A) Dominant SPW-R response profiles across probes. Each panel shows the projections of the first three principal components from a given partner area (columns) and probe (rows). Legend denotes the % explained variance of each component. For all probes and regions, the first three PCs explained more than 50% of the variance. Note the differences in magnitude and signs of response profiles across different probes. B) Fractions of significantly modulated units for each area and each probe (mean ± s.e.m.; n = 26 sessions where all 6 probes were available). C) Pie chart showing the fractions of extra-hippocampal units that are significantly modulated by SPW-Rs on probe A only, probe D only, neither or both probes. Bar graphs next to each pie slice show the fractions of units per area. Significantly more cells are modulated during SPW-R on both probes than would be expected by chance ($p = 3.5 \times 10^{-8}$; Z test for proportions). D) Bar graph showing the fractions of positively and negatively modulated units in each of group in (C). The proportion of positively modulated cells on probe A was significantly higher than negatively modulated cells (n = 2735 and 1995, respectively, significantly modulated units; $p<0.001$, chi-squared statistic=231.54). Inversely, on probe D, the proportion of negatively modulated cells was significantly higher (n = 2612 and 2568, respectively, significantly modulated units; $p<0.001$, chi-squared statistic=69.69). The fraction of A-D+, A+D+ and A-D-, but not A+D- are higher than expected by chance overlap ($p<0.001$; Z-test for proportions). E) Regression lines for the linear regression between SPW-R modulation of all extra-hippocampal units by probe A and D (n = 34 sessions were both probes were available). Note that in nearly every session target units were more strongly correlated with SPW-Rs of the septal than posterior sites.

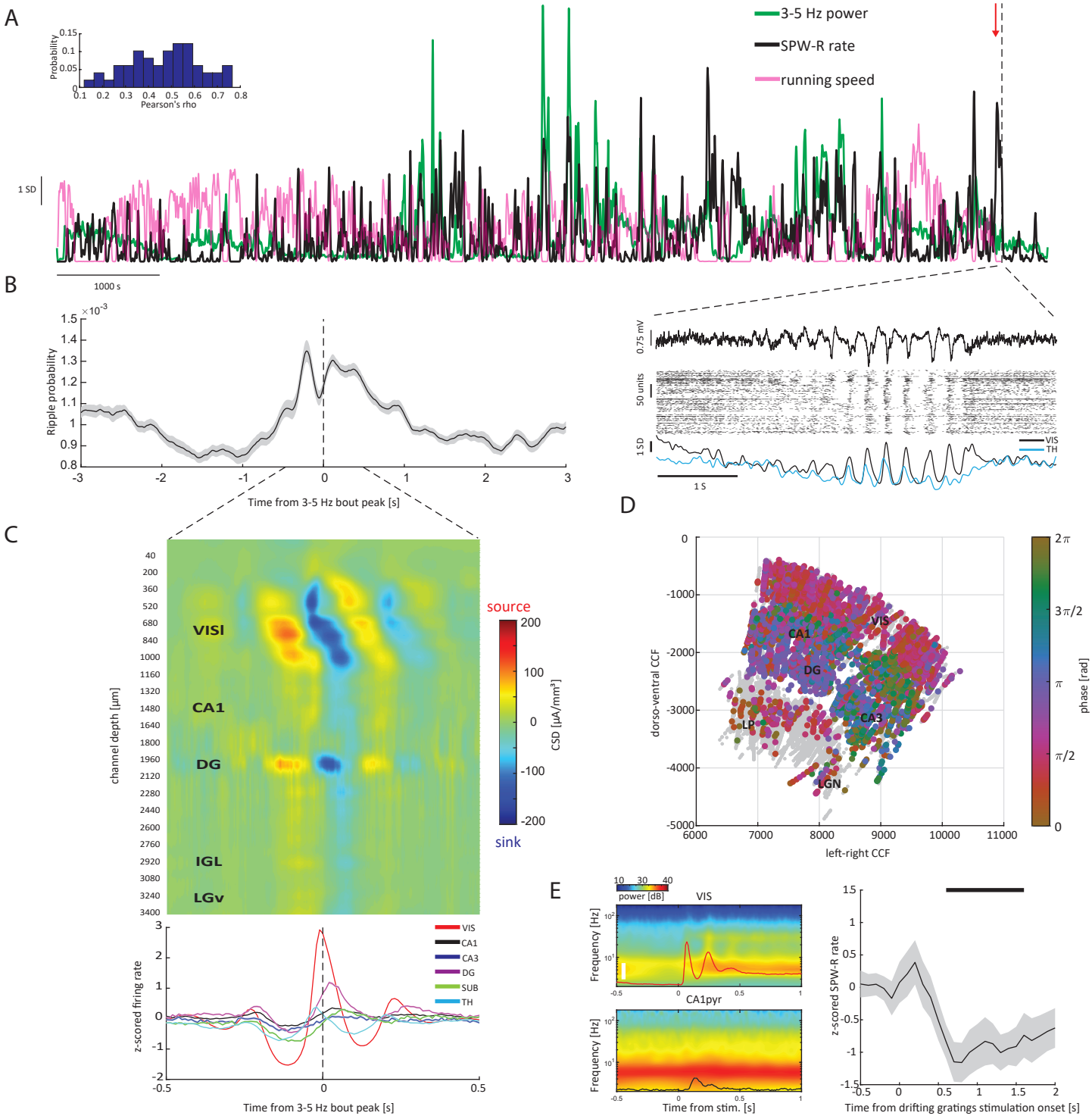
A
3-5 Hz power
SPW-R rate
running speed
Probability
Pearson's rho
1 SD
1000 s
B
Ripple probability
Time from 3-5 Hz bout peak [s]
0.75 mV
50 units
1 SD
VIS
TH
1 S
C
VISl
CA1
DG
IGL
LGv
channel depth [µm]
source
sink
CSD [µA/mm³]
z-scored firing rate
VIS
CA1
CA3
DG
SUB
TH
Time from 3-5 Hz bout peak [s]
D
dorso-ventral CCF
left-right CCF
phase [rad]
LP
LGN
E
power [dB]
Frequency [Hz]
CA1pyr
Time from stim. [s]
z-scored SPW-R rate
Time from drifting gratings stimulation onset [s]

Fig. S8. Dominant 4 Hz oscillation in visual cortex biases hippocampal activity. A) Top: Normalized 3-5 Hz power (green) and instantaneous SPW-R rate (black, obtained from convolving SPW-R peak times with a 5 SD Gaussian kernel) and running speed (smoothed with a 5 SD Gaussian kernel for visualization) from one example session (session ID: 715093703). Red arrow, last stimulation. Top left inset: Distribution of correlation values between SPW-R rate and 3-5 Hz power from all sessions. Bottom right inset: Example spontaneous event showing LFP from a supragranular visual cortex channel (top), the concomitant raster plot of all visual cortex units (middle) and summed MUA from visual cortex (black) and thalamus (cyan). Note that thalamic unit firing leads waves of the 4 Hz episode. B) Distribution of SPW-R probability (mean ± s.e.m.) triggered by the peaks of integrated 3-5 Hz bouts peak, restricted to epochs not including grating stimulations (n = 45 sessions with >500 events). C) Top: CSD plot averaged across all 3-5 Hz events from one example session. Note the phase-shifting of current sink from superficial to deep layers of the visual cortex. Note also a prominent sink in the dentate molecular layer. Bottom: PSTHs (mean ± s.e.m.) showing z-score normalized firing rates of visual cortical, hippocampal and thalamic (TH) units around 3-5 Hz bout peaks (CA1, n = 5840; CA3, n = 841; DG, n = 1627; SUB, n = 1481; TH, n = 6341). Note earliest firing peak in thalamus. Note also recruitment of dentate gyrus units. D) Coronal view of preferred 3-5 Hz spike phase, referenced to superficial visual cortical LFP recorded on probe A. Non significantly modulated units are shown in grey (n = 7808/36156, Rayleigh test for circular non-uniformity). E) Left: average spectrogram from one example session (session ID: 732592105) centered around drifting grating stimulation onset from a visual cortex channel (top) and a CA1 str. pyramidale channel (bottom). The respective PSTHs are superimposed (mean ± s.e.m.; n = 18,081 units from 25 sessions). White scale bar, 1 SD. Right: Averaged z-scored SPW-R rate centered around drifting gratings stimulation onset. SPW-Rs rate was reduced following stimulation. Black bar indicates significantly reduced bins. (Bonferroni corrected rank sum test, n = 25 sessions). The correlation between 4 Hz visual cortical bouts and SPW-R rate may be explained by reduced attention (habituation) during stimulation session.

SI References

1. N. A. Steinmetz, P. Zatka-Haas, M. Carandini, K. D. Harris, Distributed coding of choice, action and engagement across the mouse brain. *Nature*, 1–8 (2019).
2. M. Sosa, H. R. Joo, L. M. Frank, Dorsal and Ventral Hippocampal Sharp-Wave Ripples Activate Distinct Nucleus Accumbens Networks. *Neuron* **105**, 725-741.e8 (2020).
3. K. H. Pettersen, A. Devor, I. Ulbert, A. M. Dale, G. T. Einevoll, Current-source density estimation based on inversion of electrostatic forward solution: Effects of finite extent of neuronal activity and conductivity discontinuities. *J. Neurosci. Methods* **154**, 116–133 (2006).
4. J. H. Siegle, *et al.*, Survey of spiking in the mouse visual system reveals functional hierarchy. *Nature*, 1–7 (2021).
5. R. Gao, E. J. Peterson, B. Voytek, Inferring synaptic excitation/inhibition balance from field potentials. *Neuroimage* **158**, 70–78 (2017).
6. A. Luczak, P. Bartho, K. D. Harris, Gating of Sensory Input by Spontaneous Cortical Activity. *J. Neurosci.* **33**, 1684–1695 (2013).
7. N. Nitzan, *et al.*, Propagation of Hippocampal Ripples to the Neocortex by Way of a Subiculum-Retrospleanial Pathway. *Nat. Commun.* **11**, 1–17 (2020).
8. J. Ho, T. Tumkaya, S. Aryal, H. Choi, A. Claridge-Chang, Moving beyond P values: data analysis with estimation graphics. *Nat. Methods* **16**, 565–566 (2019).
9. F. Claudi, *et al.*, Visualizing anatomically registered data with brainrender. *Elife* **10** (2021).